Received: 27 March 2022 | Revised: 13 July 2022 | Accepted: 26 July 2022

DOI: 10.1002/er.8515

RESEARCH ARTICLE

INTERNATIONAL JOURNAL OF ENERGY RESEARCH WILEY

Thermodynamic modeling of a spectrum split perovskite/silicon solar cell hybridized with thermoelectric devices

Mkpamdi N. Eke[1,2] | **Onyebuchi I. Ibeagwu**[1] | **Edmund C. Okoroigwe**[1] | **Chika C. Maduabuchi**[2,3]

[1]Department of Mechanical Engineering, University of Nigeria, Enugu, Nigeria

[2]Africa Centre of Excellence for Sustainable Power and Energy Development, University of Nigeria, Nsukka, Nigeria

[3]Department of Nuclear Science and Engineering, Massachusetts Institute of Technology, Cambridge, Massachusetts, USA

Correspondence

Onyebuchi I. Ibeagwu, Department of Mechanical Engineering, University of Nigeria, Nsukka 410001, Enugu, Nigeria.
Email: onyebuchi.ibeagwu@unn.edu.ng

Chika C. Maduabuchi, Department of Nuclear Science and Engineering, Massachusetts Institute of Technology, Cambridge, MA 02139, USA.
Email: chika691@mit.edu

Summary

To facilitate the attainment of higher performance in the tandem perovskite/silicon solar cell, this work seeks to conduct the thermodynamic modeling and analysis of a spectrum splitting tandem perovskite/silicon solar hybridized with thermoelectric (TE) devices. A dichroic beam splitter is employed as the solar concentrator for the utilization of the entire solar spectrum and the effects of temperature dependency and leg geometry alteration are considered in the TE device pins. Additionally, a TE cooler (TEC) is lapped behind the backplate of the tandem solar cell to reduce overheating and allow for higher power generation from the hybrid system. Finally, novel equations are developed to study the effects of varying the halide composition of the perovskite on the overall system performance. Among several fascinating results obtained, it was disclosed that increasing the bromine composition only improved the system's performance when a halide composition of 0.2 was used for hybrid organic-inorganic perovskite thickness ranging from 300 to 400 nm. It was also forecasted that as the solar cells are exposed to higher concentrated solar irradiances, the effects of increasing the halide composition on the system's performance will become more notable. Additionally, utilizing a TEC to maintain the tandem solar cell backplate temperature at 293K is not beneficial to the system's performance when a beam splitter is used. Finally, it was found that the highest system efficiency of 42% was obtained at a split wavelength of 800 nm which is considerably higher than the 23.6% reported for standalone perovskite/Si. These results are sufficient to provide useful insights regarding the operation of spectrum splitting tandem perovskite/silicon solar cells with TE devices.

KEYWORDS

halide composition, spectrum splitter, tandem perovskite/silicon solar cell, thermodynamic modeling, thermoelectric cooler, thermoelectric generator

1 | INTRODUCTION

1.1 | General overview on photovoltaics

The use of photovoltaic (PV) modules is on the increase due to the clean energy they provide relative to greenhouse gas emissions from fossil fuel sources like coal-fired power plants.[1] Additionally, the fear that fossil fuel sources will soon be exhausted, due to the exponentially increasing human population, has accelerated the search for efficient alternate energy sources.[2] However, the sensitivity of solar cells to light and temperature causes a severe reduction in the PV module efficiency.[3] This is why previous works sought to mitigate the efficiency reduction of PVs by combining them with different solid-state energy devices which convert the waste heat to useful electricity.[4] Due to the adverse effects of high temperature on the PV module, spectrum splitters were utilized to split the concentrated beam into individual energy components.[5] The major components are short wavelengths for the PV module (such as ultraviolet and visible light) and long wavelengths (near-infrared and infrared) for the solid-state energy converters.[6]

1.2 | Benefits of tandem perovskite/silicon solar cells

Research has shown that higher efficiencies are obtainable by increasing the number of stalked PV cells.[7] The major objective in the design of PV solar cells is to maximize the efficiency-to-cost ratio. Perovskite solar cells (PSCs) have reasonably met that requirement.[8] Efficiencies of lead halide-based PSCs has rapidly been improved, reaching 20% on small-area devices making this material a competitive thin-film PV technology.[9] Furthermore, recent research has shown that introducing a mixture of bromide and iodide in the halide composition of lead methylammonium perovskites allows for continuous fine-tuning of the band gap which is a fine property for multi-junction solar cells.[10] The major variations of tandem device configuration for solar cells are the perovskite-perovskite and perovskite-silicon tandem solar cells.[11] The perovskite-perovskite configuration has a lower greenhouse gas emission factor and energy payback time compared to the silicon benchmark. Also, the thermodynamic efficiencies of the perovskite-perovskite and perovskite-silicon tandem solar cells are very high (exceeding 30%), thus, paving the way for upgrading the silicon cell performance at little extra cost in short-term and long-term basis, respectively.[12] Perovskite/Si combination as tandem solar cells is of great interest due to the possibility of boosting efficiencies above 30% while reducing the cost per kilowatt hour (kWh).[13] Futscher and Ehrler[14] indicated that perovskite/Si at different locations may require different tandem configuration and/or perovskite band gaps to minimize the cost per kWh. They also showed that by using a perovskite top cell with the ideal band gap for the respective tandem configuration, perovskite/Si with power conversion efficiency limits above 41% is possible for all three tandem configurations even at non-ideal climate conditions. Al-Alshouri et al.[15] reported a tandem monolithic perovskite/Si solar cell with a record-breaking efficiency of 29.15%. The absorber of the perovskite cell was made to remain stable when exposed to illumination via a series of very fast extraction of holes and minimization of nonradiative recombination at selected hole interfaces. Kim et al.[16] designed and developed a bifacial 4-terminal tandem perovskite/Si heterojunction solar cell that generated 30% efficiency. The efficiency recorded by the hybrid bifacial solar cell was greater than the 29.43% Schockley-Quiesser limit for crystalline-based Silicon solar cells. He et al.[10] achieved a 29.5% efficiency from a tandem heterojunction perovskite/Si solar cell with a 1.74 eV open circuit voltage from the top and bottom cells of the device. They further reported that adding methylammonium chloride reduced the device open circuit voltage in the PSC while the Lead Iodide helps in increasing the open-circuit voltage by playing a passivation role. Li et al.[17] noted that the high conversion efficiencies obtained from tandem perovskite/Si solar cells were due to the advantages of perovskite materials such as their low cost, tunable bandgaps, and easy fabrication.

1.3 | Thermoelectric devices applied in tandem PVs

Thermoelectric (TE) modules are solid-state energy conversion devices that directly convert thermal energy to electricity based on TE effects.[18] These devices offer several desirable perks such as solid-state and noiseless operation, environmental friendliness, and zero maintenance costs.[19] Due to their harnessing of the TE effects to convert thermal energy, they have found various applications in converting waste heat in several power systems to electricity.[20] More specifically, they have proven to be good companions with PV systems in hybrid designs such as the PV-thermoelectric generators (TEGs)[21] and PV-TE coolers (TECs).[22] However, PV-TEC sandwiched module has shown improved the efficiency and the overall power output of the hybrid system due to the Peltier cooling process.[23] In addition, PV-TEG hybrid system with a beam splitter demonstrated higher efficiency in comparison to the sandwiched system[24] due to the conversion of

waste heat from the back plate to electric output. In addition, some authors[25] hybridized the PV-TEG system with single junction PV and beam splitters to enable spectrum management and reduce the thermal losses encountered in the direct coupling/sandwiching method.

The emerging high-efficiency PSC has also been combined with TEGs to form hybrid generating systems capable of utilizing the broad solar spectrum.[26] Zhang et al.[27] estimated the features and feasibility of directly coupling a PSC with TE modules and reported that the efficiencies obtained from the hybrid and standalone systems were 18.6% and 17.8%, respectively, for a temperature coefficient that was lower than 2%. It was further shown that the PSC is a very suitable option for the PV-TEG system. Xu et al.[28] optimized the performance of a splitting PSC integrated with a TEG and recorded an efficiency of 20.3% after optimizing the performance of the device. The hybrid device was operated under AM 1.5G conditions, an open-circuit voltage of 1.29 V, and an irradiance of 100 mW cm^{-2}. Liao et al.[29] recorded efficiencies of 20.4%, 5.16%, and 20.8% for a standalone PSC, TEG, and hybrid PSC-TEG system, respectively. After optimizing the operating parameters of the PSC-TEG system, the hybrid device was able to realize a maximum efficiency of 22.9% for an optimum layer thickness of 449.7 nm. It was finally stated that incorporating the TEG in the PSC facilitated the reduction of waste heat emission and improvement of the power and conversion efficiency of the PSC. Zhou et al.[7] utilized a TEG in reducing the heat generation process in a concentrated PV system made of metal-halide PSC. At a concentrated solar irradiance of 3 suns, the hybrid system was able to achieve a maximum efficiency of 35%, which was 4.7% higher than that of the standalone PSC. Finally, Lorenzi et al.[30] showed that relative to the amorphous Silicon and Gallium Indium Phosphide cells, the PSC showed a maximum efficiency enhancement of 3.1% when a bismuth-telluride based TEG was operated in tandem. Based on their results, they further concluded that the PSC has a greater potential of harnessing waste heat via TEGs compared to the popular Si solar cells. However, no efforts have been made to combine the hybrid PSC/Si system with TE devices so as to improve the system efficiency by reducing the overheating of the tandem cells.

1.4 | Scientific novelty

The literature review shows the potential of the PSC in utilizing the broad solar spectrum by incorporating TE devices. Furthermore, the emerging tandem PSC/Si system is showing very promising power densities and efficiencies due to the deposition of perovskite in the Si layers. However, it has been found that the efficiency of the tandem PSC/Si system is strongly affected by spectral and temperature changes as well as the composition of the halide. Up to date, no effort has been made to mitigate the effects of spectral, temperature, and halide composition on the efficiencies of tandem PSC/Si systems.

This work is novel in many ways. First, a thermodynamic modeling of a concentrated tandem PSC/Si system combined with a spectrum splitting TEG having trapezoidal leg geometry is presented. The spectrum splitting system used is a dichroic beam splitter which allows the TEG to utilize the infrared region which is detrimental to the efficiency of the hybrid PSC/Si system. Second, in a bid to modify and increase the utilizable spectrum, the hybrid PSC/Si system is coupled to a TEC to reduce the thermal heating of the system for improved power generation and demonstration of the halide proportion. Finally, the effects of varying the halogen composition are studied so as to better understand the effect of its tunable band gap energy.

2 | METHODOLOGY

In this section, the detailed descriptions of the hybrid PSC/Si tandem system operated with TE devices are presented in Section 2.1. Then, Section 2.2 shows the model equations used to describe the performance of the various components making up the spectral splitting hybrid device.

2.1 | Description of the conceptualized system

The proposed hybrid system as shown in Figure 1 consists a dichroic spectrum splitter, concentrator, perovskite/Si tandem solar cells, trapezoidal TEG, and TEC. These components are added to improve the performance of the overall system. TEG can directly convert thermal energy into electric power. Radiation energy near the bandgap is directly converted to electricity by PV panel and simultaneously, infrared energy is utilized by the TEG to convert heat to electricity. Consequently, more electricity can be produced by the hybrid system than the electricity produced by a single PV or TE system.

The tandem PV device is sandwiched with the thermoelectric cooler and a co-receiver of the concentrated split light beam with the trapezoidal leg generator. As certain fraction of the incoming solar irradiance, incidents on the surface of both solid-state converters, heat is being lost to the atmosphere through convection and radiation from both top and back surfaces.

2.2 | Modelling equation formulation

For a wavelength range of 280 4000 nm and the cutoff or split wavelength λ_s, the total concentrated irradiance into the entire system is given[31] as

$$Q_{SP}+Q_{SE}=\int_{280nm}^{\lambda_s}\eta_{opt}A_{pv}CG(\lambda)d\lambda+\int_{\lambda_s}^{4000nm}\eta_{opt}A_{TEG}CG(\lambda)d\lambda \tag{1}$$

where all terms in Equation (1) are defined in the nomenclature.

2.2.1 | Analysis of the trapezoidal TEG

The footprints of the TEG are known to be of great importance in the modeling and performance of a TEG. Geometric parameters of the TEG (eg, thermoelement leg length and cross-sectional area) can influence the performance of a hybrid system. For the trapezoidal geometry under study, the length which is dependent the cross-sectional area of the TEG is shown in Figure 2 is expressed by[20] as in Equation (2).

$$A(x)_{trap-leg}=\frac{A_0-A_1}{L}x+A_1=A^*x+A_1 \tag{2}$$

The one-dimension energy balance of the trapezoidal leg for an infinitesimal element, yields for the p and n-type leg, respectively, as given by Equation (3).[32,33]

$$\frac{d}{dx}\left(k_pA(x)\frac{dT_p}{dx}\right)-\tau_pI_{TEG}\frac{dT_p}{dx}=-\frac{I_{TEG}^2\rho_p}{A(x)} \tag{3}$$

$$\frac{d}{dx}\left(k_nA(x)\frac{dT_n}{dx}\right)+\tau_nI_{TEG}\frac{dT_n}{dx}=-\frac{I_{TEG}^2\rho_n}{A(x)} \tag{4}$$

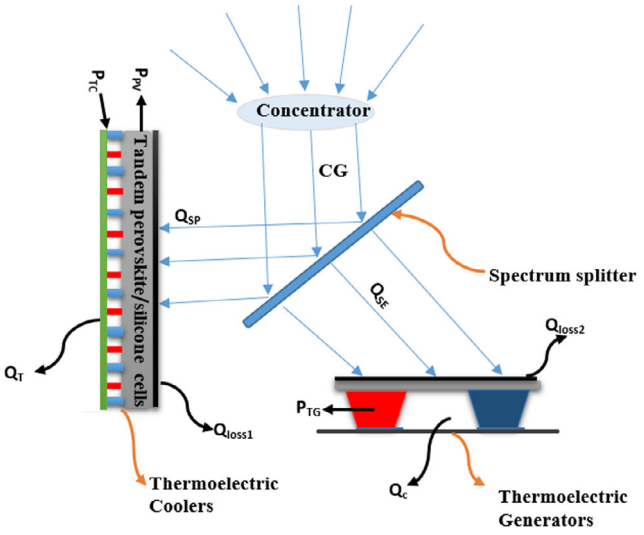

FIGURE 1 Schematic of the hybrid system

where the parameters in all equations are defined in the nomenclature. The thermal conductivity can be replaced with a mean value within the junction temperature range and treating it as a constant while differentiating and rearranging Equations (2)–(4) gives

$$A(x)^2\frac{d^2T_p}{dx^2}+A(x)\left[\frac{A^*}{L}-\frac{\tau_pI_{TEG}}{\widetilde{k}_p}\right]\frac{dT_p}{dx}=-\frac{I_{TEG}^2\rho_p}{\widetilde{k}_p} \tag{5}$$

$$A(x)^2\frac{d^2T_n}{dx^2}+A(x)\left[\frac{A^*}{L}+\frac{\tau_nI_{TEG}}{\widetilde{k}_n}\right]\frac{dT_n}{dx}=-\frac{I_{TEG}^2\rho_n}{\widetilde{k}_n} \tag{6}$$

The differential Equations (5) and (6) can be solved by applying the principle of superposition using the Euler-Cauchy and Wronskian approach for the complementary and particular solutions. These two equations result to

$$T_p(x)=c_1+c_2\left[\frac{A^*}{L}x+A_0\right]^{-\frac{\tau_pI_{TEG}}{k_p}}+\frac{I_{TEG}\rho_pL}{\tau_pA^*}\left\{\left[\frac{A^*}{2L}x^2+A_0x\right]+\frac{L\widetilde{k}_p}{A^*\left(2\widetilde{k}_p+\tau_pI_{TEG}\right)}\left[\frac{A^*}{L}x+A_0\right]^2\right\} \tag{7}$$

$$T_n(x)=c_3+c_4\left[\frac{A^*}{L}x+A_0\right]^{-\frac{\tau_nI_{TEG}}{k_p}}+\frac{I_{TEG}\rho_nL}{\tau_nA^*}\left\{\left[\frac{A^*}{2L}x^2+A_0x\right]+\frac{L\widetilde{k}_n}{A^*\left(2\widetilde{k}_n+\tau_nI_{TEG}\right)}\left[\frac{A^*}{L}x+A_0\right]^2\right\} \tag{8}$$

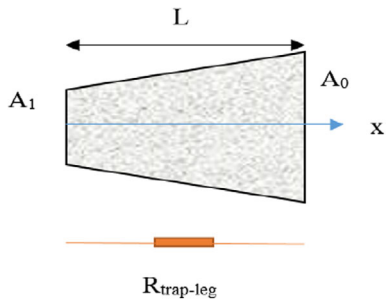

FIGURE 2 Cross section of the trapezoidal TEG leg. TEG, thermoelectric generator

The constants c_1, c_2, c_3, and c_4 in Equations (7) and (8) can be evaluated using the following boundary conditions:

$T_n(x=0)=T_p(x=0)=T_c$

and $T_n(x=L)=T_p(x=L)=T_h$

For the trapezoidal leg, considering that the geometrical parameters of both n and p-type legs are same, the internal resistance for a uni-couple or a pair is derived and expressed as

$$R_{trap-leg}=\int_0^L \frac{(\rho_p+\rho_n)dx}{\left(\frac{A_0-A_1}{L}x+A_1\right)} \tag{9}$$

$$R_{trap-leg}=\left(\widetilde{\rho}_p+\widetilde{\rho}_n\right)\left(\frac{L}{A_0-A_1}\right)\ln\left(\frac{A_0}{A_1}\right) \tag{10}$$

Since the process occurs at steady state and isolates a TEG leg, the conductive heat transfer rate in *x*-direction of Figure 2 is written as

$$Q_x=-\left(-kA(x)\frac{dT}{dx}\right)=kA(x)\frac{dT}{dx} \tag{11}$$

The negative sign indicates that the heat transfer direction is in opposite direction to the *x*-axis. Rearranging Equation (11) becomes

$$Q_x\int_0^L \frac{dx}{A(x)}=\widetilde{k}\int_{T_c}^{T_h} dT \tag{12}$$

Substituting, integrating, and incorporating the mean thermal conductivities of the pair, Equation (12) yield

$$Q_x\left[\frac{L}{A_0-A_1}\ln\frac{A_1}{A_0}\right]=\left(\widetilde{k}_p+\widetilde{k}_n\right)(T_c-T_h) \tag{13}$$

From Equation (13), the thermal conductance for the trapezoidal leg is given as

$$K_{trap-leg}=\frac{\widetilde{k}_p+\widetilde{k}_n}{\left[\frac{L}{A_0-A_1}\ln\left(\frac{A_0}{A_1}\right)\right]} \tag{14}$$

The overall energy balance for the entire solar TEG in Figure 1 gives,

$$Q_{SE}-\rho Q_{SE}-Q_{radTG}-Q_{convTG}=P_{TG}+{}^{TG}Q_c \tag{15}$$

$$\alpha_{TG}Q_{SE}-Q_{radTG}-Q_{convTG}=P_{TG}+{}^{TG}Q_c \tag{16}$$

For the selective absorber, energy balance is also given as

$$\alpha_{TG}\int_{\lambda_s}^{4000nm}\eta_{opt}A_{TEG}CG(\lambda)d\lambda-Q_{radTG}-Q_{convTG}={}^{TG}Q_h \tag{17}$$

The heat absorbed at the TEG hot junction is given by equation (18)

$${}^{TG}Q_h=N\Big\{S_hI_{TEG}T_h-0.5I_{TEG}^2R_{trap-leg}+K_{trap-leg}(T_h-T_c)-0.5\tau_{TEG}I_{TEG}(T_h-T_c)\Big\} \tag{18}$$

The radiation and convective heat terms can be replaced with an equivalent heat quantity. Substituting Equation (18) into Equation (17) gives the expression in Equation (19)

$$\alpha_{TG}\int_{\lambda_s}^{4000nm}\eta_{opt}A_{TEG}CG(\lambda)d\lambda-A_{TEG}h_0(T_h-T_a)=\left\{\begin{matrix}N\left[S_hI_{TEG}T_h-0.5I_{TEG}^2R_{trap-leg}\right]+\\N\left[k_{trap-leg}(T_h-T_c)-0.5\tau_{TEG}I_{TEG}(T_h-T_c)\right]\end{matrix}\right\} \tag{19}$$

The electrical current of the TEG with Thomson influence considered is given as

$$I_{TEG}=\frac{N(S_hT_h-S_cT_c-\tau_{TEG}(T_h-T_c))}{R_L+NR_{trap-leg}} \tag{20}$$

Substituting Equation (20) into Equation (19) and simplifying gives

$$\frac{1}{R_L + NR_{trap-leg}}\left[\zeta''' T_h^2 + \zeta'' T_h\right] + \zeta' = 0 \tag{21}$$

where ζ''', ζ'', and ζ' are respectively expressed as

$$\zeta''' = \left\{ \begin{array}{l} 0.5NR_{trap-leg}\left(\dfrac{N^2S_h^2 - 2\tau_{TEG}N^2S_h + N^2\tau_{TEG}^2}{R_L + NR_{trap-leg}}\right) - \\ \left(N^2S_h^2 - 1.5\tau_{TEG}N^2S_h + 0.5N^2\tau_{TEG}^2\right) \end{array} \right\} \tag{22}$$

$$\zeta'' = \left\{ \begin{array}{l} 0.5NR_{trap-leg}\left(\dfrac{2NS_hT_c[\tau_{TEG}N - NS_c] - 2N\tau_{TEG}T_c[\tau_{TEG}N - NS_c]}{R_L + NR_{trap-leg}}\right) + \\ \left(-0.5N^2\tau_{TEG}S_hT_c + 0.5N^2\tau_{TEG}^2T_c\right) - \\ \left(A_{trap-leg}h_0 + NK_{trap-leg}\right) + \left(N^2S_cS_h - N^2\tau_{TEG}S_h - 0.5N^2\tau_{TEG}S_c + 0.5N^2\tau_{TEG}^2\right)T_c \end{array} \right\} \tag{23}$$

$$\zeta' = \left\{ \begin{array}{l} \dfrac{1}{R_L + NR_{trap-leg}}\left\{\left[0.5N^2\tau_{TEG}S_cT_c^2 - 0.5N^2\tau_{TEG}^2T_c^2\right] + \dfrac{0.5NR_{trap-leg}[\tau_{TEG}N - NS_c]^2T_c^2}{R_L + NR_{trap-leg}}\right\} + \\ \alpha_{TG}\displaystyle\int_{\lambda_s}^{4000nm} \eta_{opt}A_{TEG}CG(\lambda)d\lambda + A_{TEG}h_0T_a + NK_{trap-leg}T_c \end{array} \right\} \tag{24}$$

The component efficiency of the trapezoidal TEG is given by Equation (25)

$$\eta_{TEG} = \frac{P_{TG}}{\displaystyle\int_{\lambda_s}^{4000nm} \eta_{opt}A_{TEG}CG(\lambda)d\lambda} \tag{25}$$

The thermal conductivity and electrical conductivity of the mid/high-temperature semiconductor (Skutterudite) used to model the TE legs are provided in Table 1, while Figure 3 shows the variation of the Seebeck conductivity with operating temperature.

2.2.2 | Analysis of the Hybrid Tandem PV-TEC

The analysis of the Hybrid Tandem PV-TEC with an irradiance within 280 nm to the cutoff wavelength incident on the perovskite/Si cells, powering a TEC and expected subjects—the multi-junction cells to reasonable operating temperature. There would be thermal losses through radiation by reflection and convection to the atmosphere, while giving a net power output (after accounting for the necessary power to drive the TEC). Isolating the hybrid system and taking an energy balance of the system, the energy balance is given as

$$\alpha_{PV}\int_{280nm}^{\lambda_s} \eta_{opt}A_{pv}CG(\lambda)d\lambda - Q_{radPV} - Q_{convPV} = P_{PV-TEC} + {}^{TC}Q_h \tag{26}$$

The radiation and convection heat losses can be expressed as[36]

$$Q_{radPV} + Q_{convPV} = A_{pv}h_0\left(T_{pv} - T_a\right) \tag{27}$$

Empirically, the combined transfer coefficient is represented by $h_0 = 5.7 + 3.8v$.

The quantity of heat from the TEC hot junction is given as

$${}^{TC}Q_h = \frac{T_{hh} - T_a}{R_{fin}} = N\left\{S_mI_cT_{hh} + 0.5I_c^2R_m - K_m(T_{hh} - T_{cc})\right\} \tag{28}$$

In this study, TECs are basically defined with specified characteristics such as I_{max}, V_{max}, Q_{max}, and DT_{max}. Imax is the input current that can produce the maximum temperature change, DT_{max} across the TEC module. Vmax is the DC voltage at the maximum temperature difference of DT_{max} and Q_{max} is the maximum amount of heat absorbed at the TEC cold side at $I = I_{max}$ and $DT_{max} = 0$. Utilizing these parameters, the module properties can be expressed as follows:

TABLE 1 Properties of the Skutterudite-based thermoelectric generator for temperature range of 300-600K[34,35]

Materials	Thermal conductivity ($W\ m^{-1}\ K^{-1}$)	Electrical conductivity ($\mu\Omega$ m)
Ce0.9Fe3CoSb12	1.87-1.77	10.43-12.65
Co4Sb11Ge0.4Te0.6	4.49-3.20	11.07-13.87

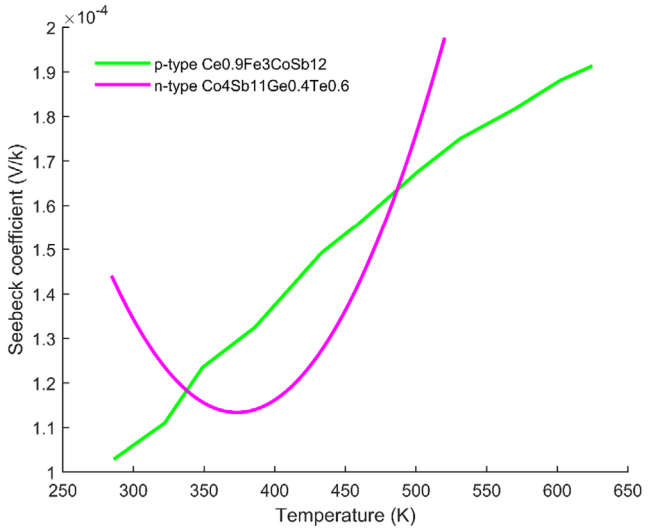

FIGURE 3 Seebeck plot of the Skutterudite-based TEG material[34,35]

$$S_m = \frac{V_{\max}}{T_a} \tag{29}$$

$$R_m = \frac{(T_a - \Delta T_{\max})V_{\max}}{T_a I_{\max}} \tag{30}$$

$$k_m = \frac{(T_a - \Delta T_{\max})V_{\max} I_{\max}}{2T_a \Delta T_{\max}} \tag{31}$$

From Equation (28), the hot junction temperature is given by

$$T_{hh} = \frac{0.5NR_{fin}I^2{}_cR_m + k_mNR_{fin}T_{cc} + T_a}{1 - NR_{fin}S_mI_c + k_mNR_{fin}} \tag{32}$$

The electrical characteristics and geometry dimensions of the TEC used in this work are provided in Table 2.

The net power output of the PV-TEC is given by Equation (33) with the TEC powered by tandem module.[38]

$$P_{PV-TEC} = P_{pv} - P_{TEC} = A_{pv}J_{sc}V_{oc}FF \tag{33}$$

To improve the conversion efficiency and enable the sub cells respond to a range of the spectrum band, multi-junction cells are interconnected in series as shown in Figure 4. As a result, the open circuit voltage and short circuit current density for multi-junction devices are given by Equations (34) and (35).[39]

$$V_{oc} = \sum_{i=1}^{n} V_{oc_i} = \sum_{i=1}^{n} V_{oc_i}1 + \frac{k_BT_{pv}}{q}\sum_{i=1}^{n} m_iIn(C) \tag{34}$$

$$J_{sc} = Min\left(C \int_{280nm}^{\lambda_s} SR_i(\lambda)\eta_{opt}G(\lambda)d\lambda\right) \tag{35}$$

where the spectral response is given by Equation (36)

$$SR_i(\lambda) = \frac{q\lambda}{hc}EQE_i(\lambda) \tag{36}$$

Substituting Equations (27), (32), (34), (35), and the last term of (28), the expression gives Equation (37)The fill factor is expressed as

$$\left\{\begin{array}{c} \alpha_{PV}\int_{280nm}^{\lambda_s}\eta_{opt}A_{pv}CG(\lambda)d\lambda \\ -A_{pv}h_0\left(T_{pv} - T_a\right) \end{array}\right\} = \left\{\begin{array}{c} A_{pv}J_{sc}FF\left(\sum_{i=1}^{n} V_{oc_i}1 + \frac{k_BT_{pv}}{q}\sum_{i=1}^{n} m_iIn(C)\right) + 0.5NI_c^2R_m + K_mT_{cc} \\ (NS_mI_c - NK_m)\left(\frac{0.5NR_{fin}I_c{}^2R_m + K_mNR_{fin}T_{cc} + T_a}{1 - NR_{fin}S_mI_c + K_mNR_{fin}}\right) \end{array}\right\} \tag{37}$$

$$FF = \frac{(\beta) - \ln(\beta + 0.72)}{(\beta + 1)} \tag{38}$$

where $\beta = \frac{qV_{oc}}{nk_BT_{pv}}$. From series expansion, natural logarithmic series of $\beta+1$ is given as

$$\ln(\beta+1) = \beta - \frac{\beta^2}{2} + \ldots \tag{39}$$

The combinations of Equations (38) and (39) can be simplified by applying numerical and analytical approaches. The fill factor can be fitted to a polynomial function using the expression

$$FF = \alpha\beta^2 + \gamma\beta + \wp \tag{40}$$

where α, γ, and $\wp$ are constants.

Substituting the expression in Equation (40) and $\beta = \frac{qV_{oc}}{nk_BT_{pv}}$ into Equation (37) and assuming the cold junction temperature of the TEC cooler to equal the tandem module temperature because the module is very thin in thickness in nanometric unit. The expression can be rearranged and simplified to give

$$\vartheta''' T_{pv}^3 + \vartheta'' T_{pv}^2 + \vartheta' T_{pv} - A_{pv}J_{sc}\alpha\left(\frac{q}{nk_B}\right)^2\left(\sum_{i=1}^{n} V_{oc_i1}\right)^3 = 0 \tag{41}$$

where ϑ''', ϑ'', and ϑ' are respectively expressed as:
The overall efficiency of the entire system comprising the multi-junction perovskite/Si, TEG, and coolers is given as

$$\eta_{sys} = \frac{A_{pv}J_{sc}V_{oc}FF - P_{TEC} + P_{TG}}{\int_{280nm}^{\lambda_s} \eta_{opt}A_{pv}CG(\lambda)d\lambda + \int_{\lambda_s}^{4000nm} \eta_{opt}A_{TEG}CG(\lambda)d\lambda} \tag{45}$$

2.2.3 | Analysis of the TE fin

For evaluating the TE fin thermal parameter, the fin thermal resistance is given as:

$$R_{fin} = \frac{1}{h_{cv}A_{eff}} \tag{46}$$

where h_{cv} and A_{eff} are respectively defined as the convective heat transfer coefficient and the effective heat transfer area of the fin. h_{cv} can be estimated using:

$$h_{cv} = \frac{N_u k_f}{H_f} \tag{47}$$

$$\vartheta''' = \left\{ \begin{array}{c} A_{pv}h_0 - A_{pv}J_{sc}\alpha\left(\frac{k_B}{nq}\right)\left(\sum_{i=1}^{n} m_i In(C)\right)^3 - A_{pv}J_{sc}\gamma\left(\frac{k_B}{nq}\right)\left(\sum_{i=1}^{n} m_i In(C)\right)^2 \\ -A_{pv}J_{sc}\frac{\wp k_B}{q}\sum_{i=1}^{n} m_i In(C) - NK_m - \frac{(NS_mI_c - NK_m)K_mNR_{fin}}{1 - NR_{fin}S_mI_c + K_mNR_{fin}} \end{array} \right\} \tag{42}$$

$$\vartheta'' = \left\{ \begin{array}{c} \int_{280nm}^{\lambda_s} \eta_{opt}A_{pv}CG(\lambda)d\lambda - 2A_{pv}J_{sc}\gamma\left(\frac{1}{n}\right)\sum_{i=1}^{n} V_{oc_i1}\sum_{i=1}^{n} m_i In(C) - \\ 2A_{pv}J_{sc}\left(\frac{2\alpha}{n^2}\right)\sum_{i=1}^{n} V_{oc_i1}\left(\sum_{i=1}^{n} m_i In(C)\right)^2 - A_{pv}J_{sc}\left(\frac{\alpha}{n^2}\right)\sum_{i=1}^{n} V_{oc_i1}\left(\sum_{i=1}^{n} m_i In(C)\right)^2 \\ -A_{pv}J_{sc}\wp\sum_{i=1}^{n} V_{oc_i1} - 0.5NI_c^2R_m - \frac{(NS_mI_c - NK_m)\left(0.5NI_c^2R_mR_{fin} + T_a\right)}{1 - NR_{fin}S_mI_c + K_mNR_{fin}} \end{array} \right\} \tag{43}$$

$$\vartheta' = \left\{ -3A_{pv}J_{sc}\left(\frac{\alpha q}{n^2k_B}\right)\left(\sum_{i=1}^{n} V_{oc_i1}\right)^2\sum_{i=1}^{n} m_i In(C) - A_{pv}J_{sc}\left(\frac{\gamma q}{nk_B}\right)\left(\sum_{i=1}^{n} V_{oc_i1}\right)^2 \right\} \tag{44}$$

TABLE 2 Properties of thermoelectric cooler[37]

I_{max} (A)	V_{max} (V)	Q_{max} (W)	ΔT_{max} (K)	Dimensions (mm)
3.7	14.7	36	66	34 × 30 × 3.4

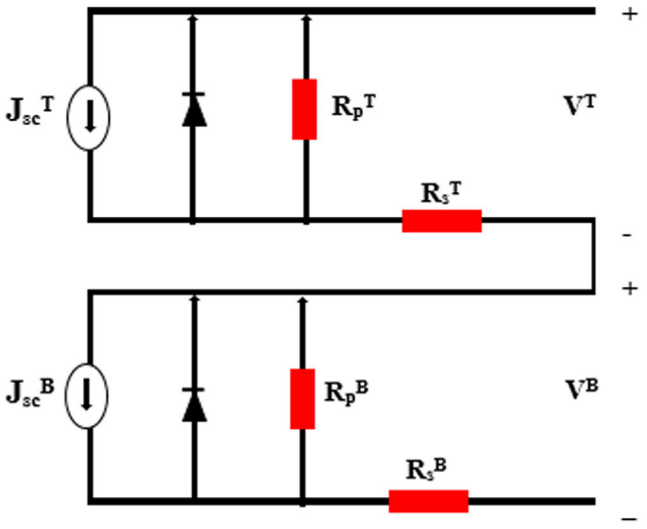

FIGURE 4 Electrical circuit of the tandem photovoltaic modules

where N_u, k_f, and k_f are the Nusselt number of the flow, the thermal conductivity of the fluid, and the height of the fins, respectively. The Nusselt number can be calculated by using the correlation for flow over a plate[40]:

$$\text{For laminar flow: } N_u = 0.664 R_e^{\frac{1}{2}} P_{rf}^{\frac{1}{3}};\ R_e < 5e10^5 \quad (48)$$

$$\text{For turbulent flow: } N_u = 0.037 R_e^{\frac{4}{5}} P_{rf}^{\frac{1}{3}};\ R_e \geq 5e10^5 \quad (49)$$

where P_{rf} and R_e are the Prandtl number of the fluid and the Reynolds number of the flow, respectively. They can be evaluated by:

$$P_{rf} = \frac{\mu_f c_{pf}}{k_f} \quad (50)$$

$$R_e = \frac{v_{ef} H_f}{\nu_f} \quad (51)$$

where μ_f, c_{pf}, k_f, v_{ef}, and ν_f are the kinematic viscosity, constant pressure heat capacity ratio, thermal conductivity, kinetic velocity, and the dynamic viscosity of the fluid, respectively. The effective heat transfer area is given by:

$$A_{eff} = \eta_f \left(2 N_f L_f H_f\right) + \left(N_f - 1\right) \delta_c L_f \quad (52)$$

where the fin efficiency η_f is given by

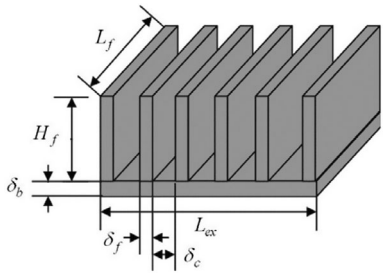

FIGURE 5 Schematic diagram of the fin[40]

$$\eta_f = \frac{\tanh\left(m H_f\right)}{m H_f} \quad (53)$$

where

$$m = \sqrt{\frac{2 h_{cv}\left(\delta_f + L_f\right)}{k_f \delta_f L_f}} \quad (54)$$

The fin geometrical properties are depicted in Figure 5 while the geometrical and thermal parameters used to define the fin in the numerical modeling equations are provided in Table 3.

2.2.4 | Modeling the halide composition variation

However, it is essential to note that the maximum wavelength, λ_{max} of the solar spectrum which can be used for the photoelectric effect differs with the computation expression as the split wavelength, λ_s varies[34]:

$$\lambda_{max} = \lambda_s \text{ where } \lambda_s < \frac{hc}{qE_g} \quad (55)$$

$$\lambda_{max} = \frac{hc}{qE_g} \text{ where } \lambda_s > \frac{hc}{qE_g} \quad (56)$$

For the perovskite $(CH_3NH_3Pb_{3(1-x)}Br_{3x}$, for $0 \leq x \leq 1$), the bandgap energy is dependent on the halide composition, x, and expressed as $E_g = 1.55 + 0.75x$; in this case, the halide is Bromine.

3 | RESULTS AND DISCUSSION

The thermodynamic modeling of a tandem perovskite/Si-TEC hybridized with a TEG module using dichroic beam

TABLE 3 Geometrical and thermal properties of the fin[40]

A_b (mm^2)	δ_b (mm)	δ_f (mm)	δ_c (mm)	H_f	N_f	P_{rf}	k_f	v_{ef} (m s^{-1})
29.7 × 29.7	2	1.3	1.3	20	12	7.02	59.9e-2	0.5

as a spectrum splitter was carried out. The study used a blend of analytical and numerical approaches utilizing the combination of MATLAB, python, and Excel spreadsheet environment. The computation was performed under a solar spectral irradiance of 1.5 air mass AM, solar concentrations ranging from 1 to 3, and fractions of the TEC maximum current as input such as $0.2I_{\max}$, $0.4I_{\max}$, $0.6I_{\max}$, and $0.8I_{\max}$. However, since perovskite cells are still undergoing material modification and this work emphasizes on what its performance would be if applied to complex system. Through numerical computations and fittings, the fill factor constants are α, γ, and $\wp$ are −0.002, 0.0706, and 0.2051. To utilize the wavelength influence on the spectral irradiance for the mathematical computation, Simpson's 3/8 rule was used to perform numerical integration on the 1.5AM spectral irradiance and the result is presented in Figure 6.

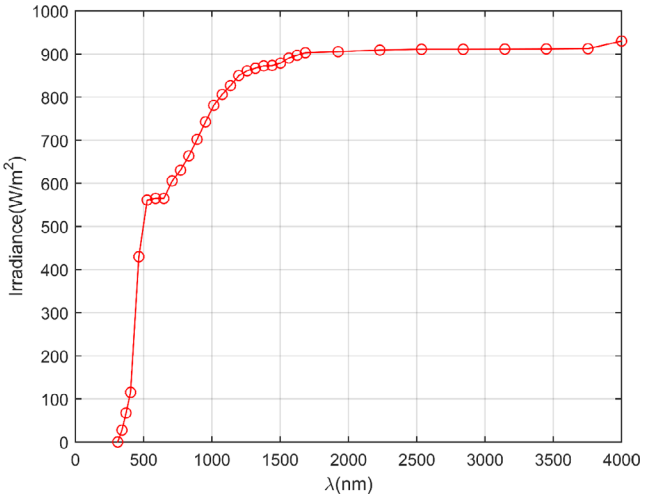

FIGURE 6 1.5AM integrated spectrum

However, for this hybrid system thermodynamic numerical analysis, the bandgap energy of the perovskite ($CH_3NH_3Pb_{3(1-x)}$ Br_{3x} (for $0 \le x \le 1$)) is dependent on the halide composition, x, which in this case is Bromine. The result of influence of the halide composition (Bromine) to the output current density of the perovskite/Si-TEC at different cell temperatures of 30°C, 35°C, 40°C, 45°C, and 50°C, concentration ratio, $C = 3$ and 0.2 of the TEC maximum current ($I_c = 0.2I_{\max}$) is shown in Table 4.

From Table 4, it was observed that the Bromine composition affects the output current density of the system. For all temperatures used (303K, 308K, 313K, 318K, and 323K), current density, J_{sc} increases as the temperature increases and reduces as the Bromine composition, x decreases. For $0.5 \le x \le 1.0$ ($1.93 \le Eg \le 2.3$), the value of the tandem module current density seems to be constant except for 303K, 318K, and 323K which showed equal absolute variation of 0.001.

The system performance for current density variation with solar irradiance and concentration factor for different TEC input current (a) $I_c = 0.2I_{\max}$; (b) $I_c = 0.4I_{\max}$; (c) $I_c = 0.6I_{\max}$; and (d) $I_c = 0.8I_{\max}$.

For all values of G and I_c ($0.2I_{\max}$, $0.4I_{\max}$, $0.6I_{\max}$, and $0.8I_{\max}$) with the tandem module held at a temperature of 293K with a split wavelength of 800 nm Figure 7a-d, the current density J_{sc}, progressively decreases as the concentration ratio increases through a nonlinear polynomial path.

The plot of current density variation with solar irradiance within a short temperature interval for different TEC input current and concentration factor $I_c = 0.2I_{\max}$, $I_c = 0.4I_{\max}$, $I_c = 0.6I_{\max}$, and $I_c = 0.8I_{\max}$ is shown in Figure 8a-d. Unlike the plots in Figure 7a-d, the group of plots shows minute variation in the temperature of the cell. Regardless of the variation in temperature, the unit value concentration still remains in the plot with the highest perovskites/Si current density values for all values of IC utilized in the computation (ie, 0.2Imax, 0.4Imax, 0.6Imax, and 0.8Imax).

The plot however is quadratic and the difference in values for the different concentration plot is small. For clarity of this statement, a plot with wider temperature range is needed as shown in Figure 9, for $0.8I_{\max}$.

The combined system efficiency dependence on the perovskite/Si-TEC current density and voltage is shown in Figure 10. From the 3D graphical plot, the plot with concentration ratio $C = 1$ has the highest efficiency amidst the three-concentration ratio (C = 1-3). From conventional PV module design, it is at least expected that the module efficiency increases after certain concentration ratio values before it begins to drop. But in this case, the graphical nature is contrary to the conventional and the reason is that beyond $C = 1$ much electrical power is required by the TEC to bring the perovskite/Si to a temperature of 293K. Carefully observing the plot, it is also seen that the planes of J_{sc} and V_{oc} have an edge trajectory that is akin to an exponential function. Viewing the plot through the efficiency and J_{sc} plane, the graph is seen to be twisted

TABLE 4 Influence of the halide composition (Bromine) on the current density of the perovskite/Si-TEC

x	0.0	0.1	0.2	0.3	0.4	0.5	0.6	0.7	0.8	0.9	1.0
Eg	1.55	1.63	1.70	1.78	1.85	1.93	2.00	2.08	2.15	2.23	2.3
303K (30°C)											
J_{sc}	5.235	5.237	5.238	5.239	5.242	5.243	5.243	5.243	5.243	5.243	5.244
308K (35°C)											
J_{sc}	5.491	5.493	5.494	5.496	5.498	5.5	5.5	5.5	5.5	5.5	5.5
313K (40°C)											
J_{sc}	5.756	5.759	5.760	5.762	5.764	5.766	5.766	5.766	5.766	5.766	5.766
318K (45°C)											
J_{sc}	6.032	6.034	6.036	6.037	6.04	6.041	6.041	6.041	6.042	6.042	6.042
323K (50°C)											
J_{sc}	6.317	6.32	6.321	6.323	6.325	6.327	6.327	6.327	6.328	6.327	6.328

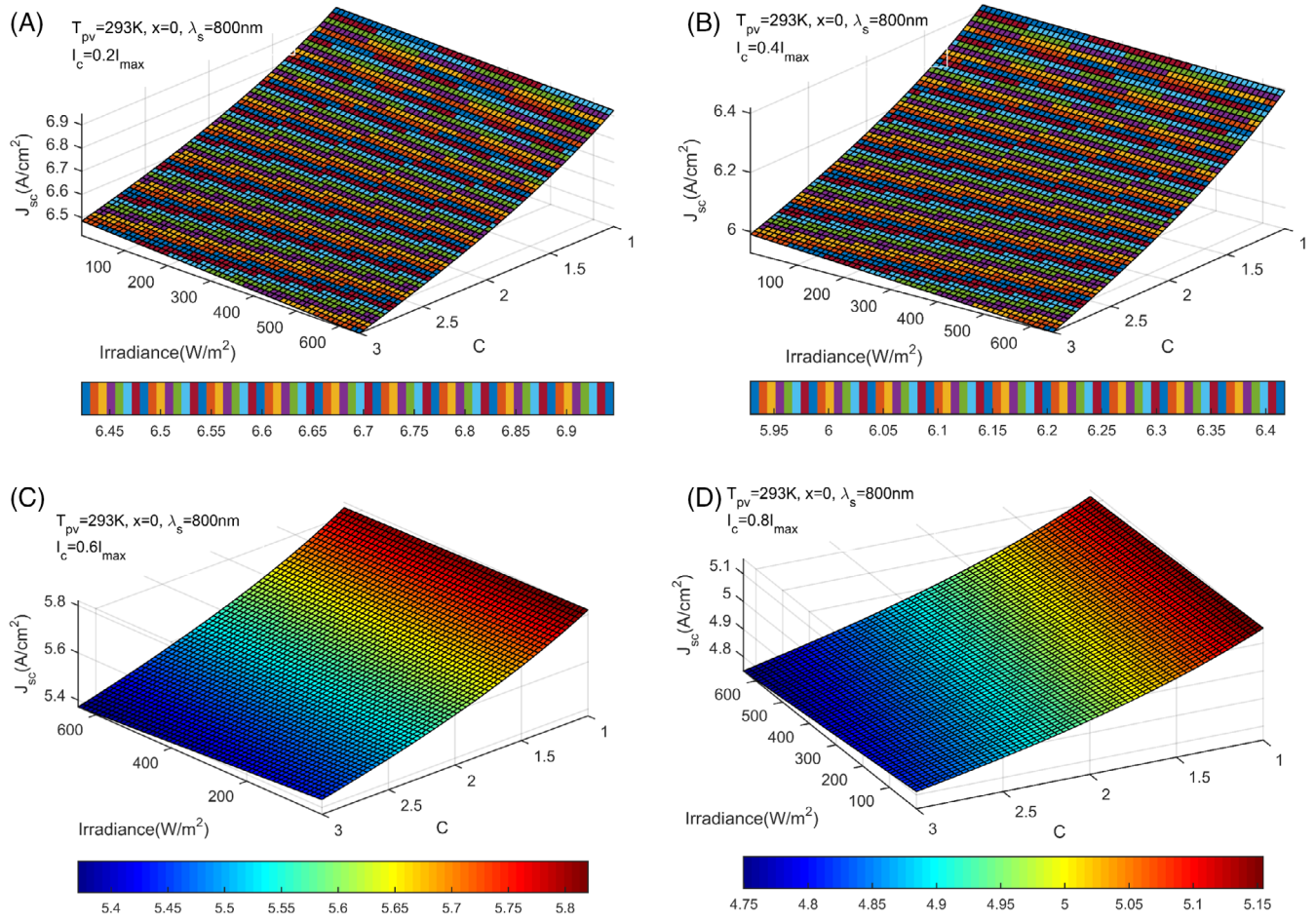

FIGURE 7 (A) Current density variation with solar irradiance and concentration factor for different TEC input current $I_c = 0.2I_{max}$. (B) Current density variation with solar irradiance and concentration factor for different TEC input current $I_c = 0.4I_{max}$. (C) Current density variation with solar irradiance and concentration factor for different TEC input current, $I_c = 0.6I_{max}$. (D) Current density variation with solar irradiance and concentration factor for different TEC input current, $I_c = 0.8I_{max}$. TEC, thermoelectric cooler

faintly and the efficiency drops as the current density increases across 6 V.

Figure 11 has a similar effect as shown in Figure 10 as much electrical power is extracted from the

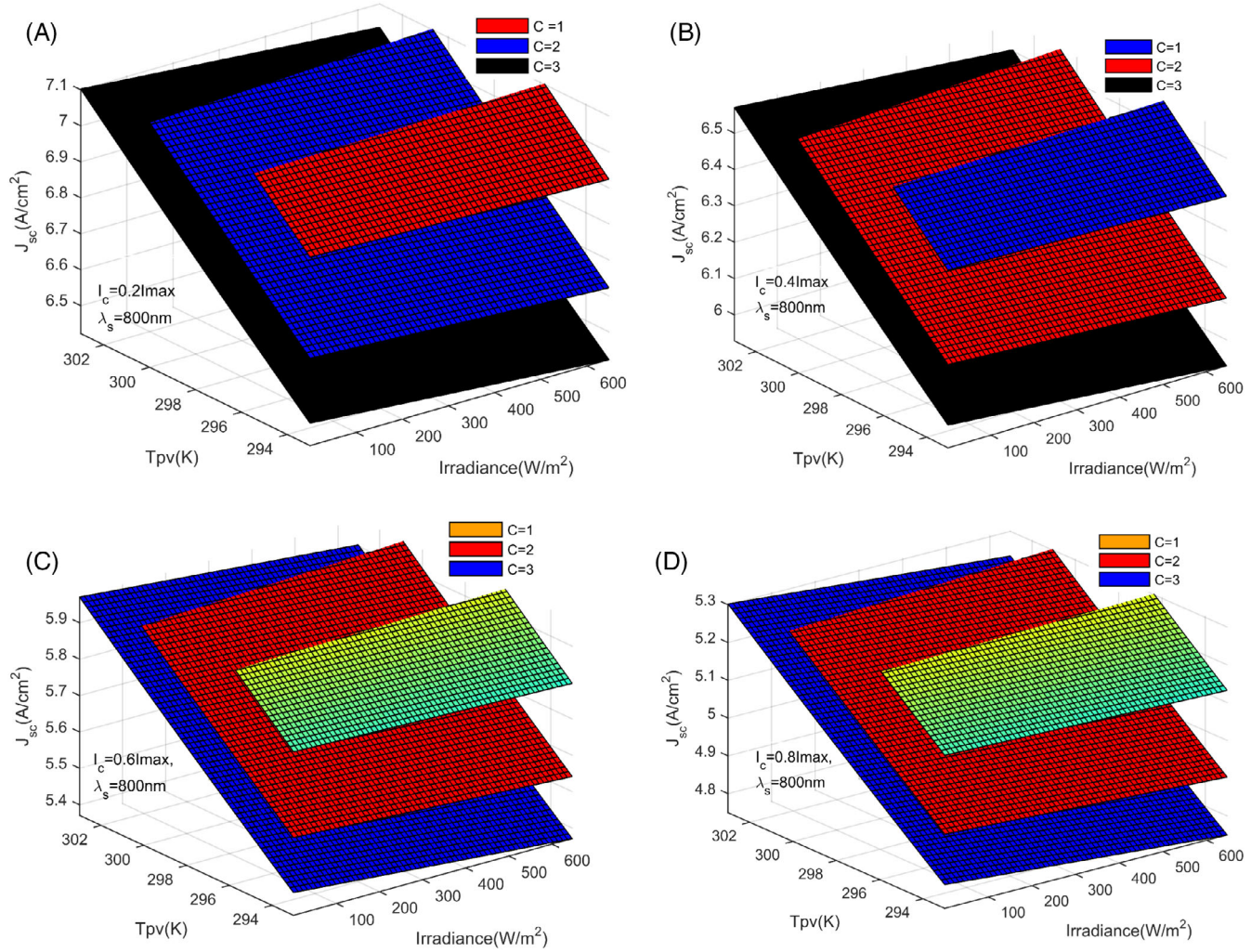

FIGURE 8 (A) Current density variation with solar irradiance within a short temperature interval for different TEC input current and concentration factor $I_c = 0.2I_{\max}$. (B) Current density variation with solar irradiance within a short temperature interval for different TEC input current and concentration factor $I_c = 0.4I_{\max}$. (C) Current density variation with solar irradiance within a short temperature interval for different TEC input current and concentration factor $I_c = 0.6I_{\max}$. (D) Current density variation with solar irradiance within a short temperature interval for different TEC input current and concentration factor $I_c = 0.8I_{\max}$. TEC, thermoelectric cooler

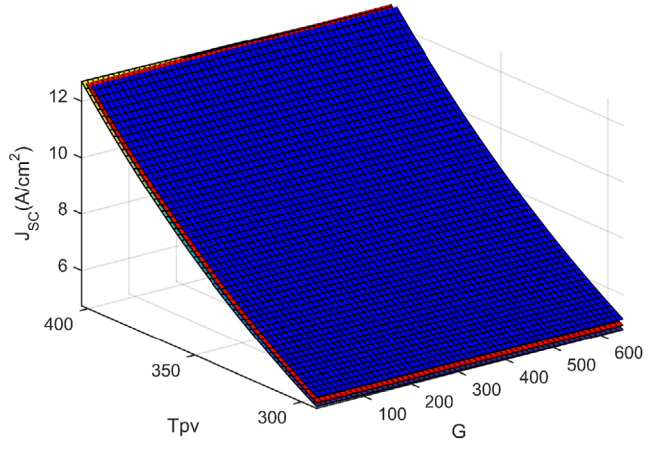

FIGURE 9 Wider temperature plot for clarity of curve nature of Figure 8

perovskite/Si module to run the TEC to sustain the PV cell temperature at 293K.

Viewing the graphical plot from the $\eta_{sys} - G$ plane, it is seen that the efficiency drops asymptotically without converging to zero as the irradiance increases. The reason for this is that at high irradiance much heat needs to be removed from the PV module to bring its temperature to 293K. For this reason, much power must be extracted and utilized by the TEC. The V_{oc} also increased progressively with a maximum combined system efficiency of about 42%. However, beyond 400 W m^{-2}, the plots were all asymptotic for all V_{oc} values. This is because the beam was split into UV and IR, and the range under consideration on the perovskite/Si, is the UV. The UV not having thermal effect but light will have temperature at the module surface within very close and low range. Therefore,

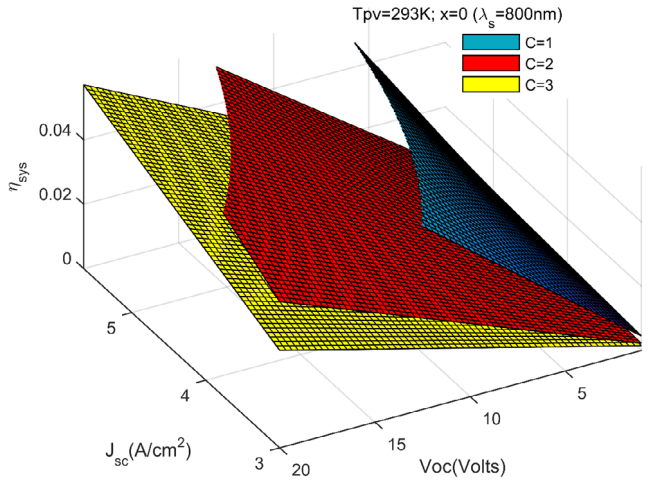

FIGURE 10 The system efficiency variation of the current density and voltage for concentration factor of *C*, 1-3

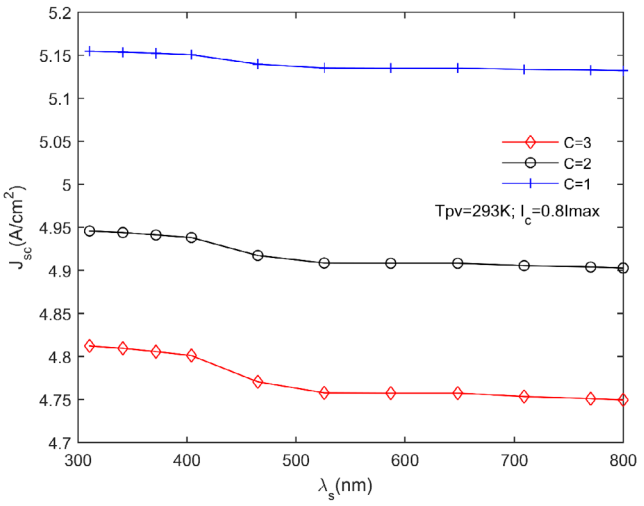

FIGURE 12 The variation of current density with cutoff wavelength

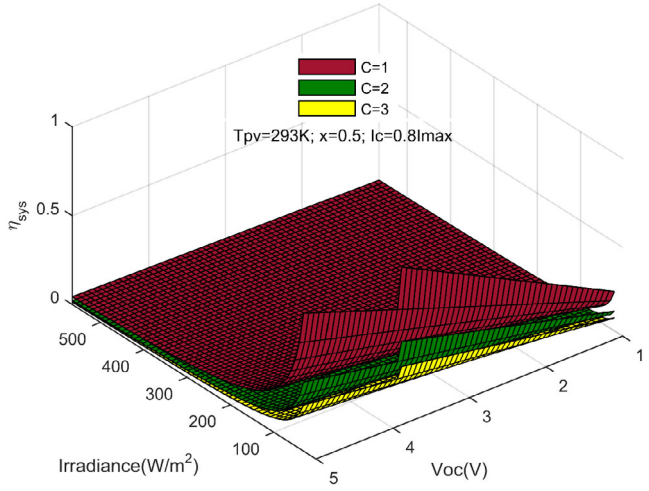

FIGURE 11 The system efficiency variation of the PV voltage for concentration factor of 1-3

small amount of electrical power would be responsible for bringing the cells under the required operating condition.

Figure 12 presents a 2D graphical plot of the perovskite/Si-TEC current density against the split/cutoff wavelength of the dichroic spectrum splitter. The plot analysis was evaluated with the perovskite/Si kept at room temperature and the TEC operating with 20% less of its maximum design current. The plot demonstrated that the perovskite/Si-TEC current density for concentration factor of 1 is higher than that of 2 and 3 with maximum values of 5.1545, 4.9458, and 4.8122 A/cm^2, respectively. Uniquely, all plots show a sharp downward slope from values range of 400 nm to 526 nm of the split wavelength. This slope emanated from the sharp increase in the solar spectrum within wavelength range of 400-526 nm (see Figure 6) and manifested downwardly because of the electric power expended by the TEC to maintain the cell at operating temperature.

In comparison with previous studies that focused on monolithic standalone perovskite/silicon solar cells that recorded maximum efficiency of 23.6%,[35] it is noticed that the proposed tandem system hybridized with TE device had a maximum efficiency of 42%. This signified that the maximum efficiency of the proposed system was 1.81 times higher than that of the previous standalone system due to the inclusion of TE devices in the hybrid system design.

4 | CONCLUSION

The thermodynamic modeling and analysis of a spectrum splitting concentrated perovskite/silicon tandem solar cell integrated with TE devices was carried out in this work to further improve the performance of the standalone perovskite/silicon solar cell. A dichroic beam splitter was used as the solar concentrator to enable the broad utilization of the entire solar spectrum. The light component from the Sun was utilized by the tandem perovskite/silicon solar cell for energy conversion while the heat component was channeled to a TEG for power generation. A TEC was directly lapped to the backplate of the tandem solar cell for temperature regulation; and consequent efficiency enhancement. The accuracy of the numerical model was ensured by accounting for temperature dependency in the variable cross-sectional area TE legs and all convective and radiative losses were fully accounted for in the developed equations. The analysis was made comprehensive enough to show the effects of

varying the halide composition on the combined system's efficiency. Based on the results obtained, the following conclusions can be made:

- A combined system efficiency of 42% was obtained from the proposed tandem perovskite/silicon solar cell integrated with TE devices when a unity solar concentration ratio was used at a split wavelength of 800 nm. This was 1.8 times higher than the efficiencies reported for standalone tandem perovskite/silicon solar cells.
- For the temperature range considered, the Bromine composition exerted a significant effect on the hybrid system's performance only for Bromine compositions varying from 0.2 to 0.5.
- For a Bromine composition of 0.2, it was observed that varying the halide composition only yielded a higher system efficiency for a wavelength range of 300-400 nm. It was also forecasted that when the hybrid system is exposed to higher concentrated solar irradiances, the significance of varying the Bromine composition becomes very notable.
- Maintaining the system's backplate temperature at 293K using a TEC was disadvantageous to the system's efficiency when a dichroic beam splitting concentrator was used. Furthermore, the power extracted from the solar cell to power the TEC was disadvantageous to the system's performance. Hence, it becomes unnecessary to use a TEC if the solar cell is operating within a functional working temperature range.

NOMENCLATURE

A_{pv}	photovoltaic surface area	m^2
A_{TEG}	thermoelectric module surface area	m^2
$A(x)_{trap-leg}$	variable thermoelectric cross-sectional area	m^2
C	optical concentration ratio	
c	speed of light	m s
$EQE(\lambda)$	external quantum efficiency	
FF	fill factor	
$G(\lambda)$	spectral irradiance	$W\ m^{-2}$
h	Plank constant	J s
h_0	radiation and convection heat transfer coefficient	$W\ m^{-2}\ K^{-1}$
I_{TEG}	thermoelectric generator current	A
J_{sc}	short circuit current density of the cell	$A\ m^{-2}$
K	Boltzmann constant	$J\ K^{-1}$
k_p	p-type thermal conductivity	$W\ m^{-1}\ K^{-1}$
k_n	n-type thermal conductivity	$W\ m^{-1}\ K^{-1}$
L	thermoelectric leg height	m
m_i	ideality factor	
P_{pv}	photovoltaic power output	W
P_{PV-TEC}	net photovoltaic output power	W
P_{TEC}	output power of thermoelectric cooler	W
P_{TG}	output power of thermoelectric generator	W
q	element charge	C
${}^{TC}Q_h$	hot junction heat of the cooler	W
${}^{TG}Q_c$	cold junction heat of the generator	W
${}^{TG}Q_h$	hot junction heat of the generator	W
Q_{convPV}	photovoltaic convective heat loss	W
Q_{convTG}	thermoelectric convective heat loss	W
Q_{radPV}	photovoltaic radiation heat loss	W
Q_{radTG}	thermoelectric radiation heat loss	W
Q_{SE}	irradiance on thermoelectric generator	W
Q_{SP}	irradiance on photovoltaic	W
$R_{trap-leg}$	thermoelectric internal resistance	Ω
$SR(\lambda)$	spectral response	$A\ W^{-1}$
T_n	n-type temperature	K
T_p	p-type temperature	K
T_{pv}	photovoltaic cell temperature	K
v	wind velocity	$m\ s^{-1}$
V_{oc}	open circuit photovoltaic voltage	Volts
α_{TG}	thermoelectric generator absorptivity	
α_{PV}	photovoltaic absorptivity	
λ_s	cutoff wavelength	nm
ρ	reflection of the selective absorber	
ρ_n	n-type electrical resistivity	Ω m
ρ_p	p-type electrical resistivity	Ω m
τ_n	n-type Thomson coefficient	$V\ K^{-1}$
τ_p	p-type Thomson coefficient	$V\ K^{-1}$
η_{opt}	optical concentrator efficiency	
η_{sys}	system efficiency	

ACKNOWLEDGMENTS

The first and last authors would like to acknowledge and appreciate the support offered by the Africa Centre of Excellence for Sustainable Power and Energy Development

(ACE-SPED), University of Nigeria, Nsukka, toward the successful completion of this work.

CONFLICT OF INTEREST

The authors declare no conflicts of interest.

DATA AVAILABILITY STATEMENT

The data used in this manuscript is available upon reasonable request from the corresponding authors.

ORCID

Chika C. Maduabuchi https://orcid.org/0000-0001-9947-5855

REFERENCES

1. Eke MN, Onyejekwe DC, Ekechukwu OV, Maduabuchi CC. Exergy and environmental assessment of a steam power plant. *Glob J Energy Technol Res Updat*. 2020;7:31-47. doi:10.15377/2409-5818.2020.07.4
2. Badillo-Ruiz CA, Olivares-Robles MA, Chanona-Perez JJ. Design of nano-structured micro-thermoelectric generator: load resistance and inflections in the efficiency. *Entropy*. 2019;21:224. doi:10.3390/e21030224
3. Aghaei M, Fairbrother A, Gok A, et al. Review of degradation and failure phenomena in photovoltaic modules. *Renew Sustain Energy Rev*. 2022;159:112160. doi:10.1016/j.rser.2022.112160
4. Rejeb O, Shittu S, Ghenai C, Li G, Zhao X, Bettayeb M. Optimization and performance analysis of a solar concentrated photovoltaic-thermoelectric (CPV-TE) hybrid system. *Renew Energy*. 2020;152:1342-1353. doi:10.1016/j.renene.2020.02.007
5. Mahmoudinezhad S, Cotfas PA, Cotfas DT, et al. An experimental study on transient response of a hybrid thermoelectric–photovoltaic system with beam splitter. *Energies*. 2021;14:8129. doi:10.3390/en14238129
6. Shittu S, Li G, Zhao X, Zhou J, Ma X, Akhlaghi YG. Experimental study and exergy analysis of photovoltaic-thermoelectric with flat plate micro-channel heat pipe. *Energ Conver Manage*. 2020;207:112515. doi:10.1016/j.enconman.2020.112515
7. Zhou Y, Chen Y, Zhang Q, et al. A highly-efficient concentrated perovskite solar cell-thermoelectric generator tandem system. *J Energy Chem*. 2021;59:730-735. doi:10.1016/j.jechem.2020.12.020
8. Ouyang Z. *Study of Thermoelectric Generators and Perovskite Solar Cells for Renewable Energy Applications*. Tuscaloosa, USA: The University of Alabama; 2020.
9. Hasan MN, Habib MM, Matin MA, Amin N. Modeling of high efficient perovskite-Si tandem solar cell. Paper presented at: 2017 International Conference on Electrical Engineering and Information Communication Technology, vol. 2018; January 2017:1-5; IEEE. doi:10.1109/EICT.2017.8275213
10. He Y, Tang Z, Mao L, et al. Minimizing open-circuit voltage loss in perovskite/Si tandem solar cells via exploring the synergic effect of cations and anions. *Phys Status Solidi – Rapid Res Lett*. 2021;15:2100119. doi:10.1002/pssr.202100119
11. Monteiro Lunardi M, Wing Yi Ho-Baillie A, Alvarez-Gaitan JP, Moore S, Corkish R. A life cycle assessment of perovskite/silicon tandem solar cells. *Prog Photovoltaics Res Appl*. 2017;25:679-695. doi:10.1002/pip.2877
12. Tian X, Stranks SD, You F. Life cycle energy use and environmental implications of high-performance perovskite tandem solar cells. *Sci Adv*. 2020;6:eabb0055. doi:10.1126/sciadv.abb0055
13. Di Giacomo F, Fakharuddin A, Jose R, Brown TM. Progress, challenges and perspectives in flexible perovskite solar cells. *Energ Environ Sci*. 2016;9:3007-3035. doi:10.1039/C6EE01137C
14. Futscher MH, Ehrler B. Efficiency limit of perovskite/Si tandem solar cells. *ACS Energy Lett*. 2016;1:863-868. doi:10.1021/acsenergylett.6b00405
15. Al-Ashouri A, Köhnen E, Li B, et al. Monolithic perovskite/silicon tandem solar cell with >29% efficiency by enhanced hole extraction. *Science (80-)*. 2020;370:1300-1309. doi:10.1126/science.abd4016
16. Kim S, Trinh TT, Park J, et al. Over 30% efficiency bifacial 4-terminal perovskite-heterojunction silicon tandem solar cells with spectral albedo. *Sci Rep*. 2021;11:15524. doi:10.1038/s41598-021-94848-4
17. Li T, Yang Y, Li G, Chen P, Gao X. Two-terminal perovskite-based tandem solar cells for energy conversion and storage. *Small*. 2021;17:2006145. doi:10.1002/smll.202006145
18. Maduabuchi C. Improving the performance of a solar thermoelectric generator using nano-enhanced variable area pins. *Appl Therm Eng*. 2022;206:118086. doi:10.1016/j.applthermaleng.2022.118086
19. Maduabuchi C, Njoku H, Eke M, Mgbemene C, Lamba R, Ibrahim JS. Overall performance optimisation of tapered leg geometry based solar thermoelectric generators under isoflux conditions. *J Power Sources*. 2021;500:229989. doi:10.1016/j.jpowsour.2021.229989
20. Maduabuchi CC, Mgbemene CA, Ibeagwu OI. Thermally induced delamination of PV-TEG: implication of Leg's Joule and Thomson heating. *J Electron Mater*. 2020;49:6417-6427. doi:10.1007/s11664-020-08390-6
21. Maduabuchi C, Lamba R, Njoku H, Eke M, Mgbemene C. Effects of leg geometry and multistaging of thermoelectric modules on the performance of a photovoltaic-thermoelectric system using different photovoltaic cells. *Int J Energy Res*. 2021;45:17888-17902. doi:10.1002/er.6925
22. Dehra H. Building-integrated thermoelectric cooling-photovoltaic (TEC-PV) devices. *Bringing Thermoelectricity into Reality*. InTech; 2018. doi:10.5772/intechopen.75472
23. Najafi H, Woodbury KA. Optimization of a cooling system based on Peltier effect for photovoltaic cells. *Sol Energy*. 2013;91:152-160. doi:10.1016/j.solener.2013.01.026
24. Mahmoudinezhad S, Cotfas DT, Cotfas PA, et al. Experimental investigation on spectrum beam splitting photovoltaic–thermoelectric generator under moderate solar concentrations. *Energy*. 2022;238:121988. doi:10.1016/j.energy.2021.121988
25. Sripadmanabhan Indira S, Vaithilingam CA, Chong KK, et al. A review on various configurations of hybrid concentrator photovoltaic and thermoelectric generator system. *Sol Energy*. 2020;201:122-148. doi:10.1016/j.solener.2020.02.090

26. Liu Z, Sun B, Zhong Y, et al. Novel integration of carbon counter electrode based perovskite solar cell with thermoelectric generator for efficient solar energy conversion. *Nano Energy*. 2017;38:457-466. doi:10.1016/j.nanoen.2017.06.016
27. Zhang J, Xuan Y, Yang L. A novel choice for the photovoltaic-thermoelectric hybrid system: the perovskite solar cell. *Int J Energy Res*. 2016;40:1400-1409. doi:10.1002/er.3532
28. Xu L, Xiong Y, Mei A, et al. Efficient perovskite photovoltaic-thermoelectric hybrid device. *Adv Energy Mater*. 2018;8:1-5. doi:10.1002/aenm.201702937
29. Liao T, He Q, Xu Q, Dai Y, Cheng C, Ni M. Performance evaluation and optimization of a perovskite solar cell-thermoelectric generator hybrid system. *Energy*. 2020;201:117665. doi:10.1016/j.energy.2020.117665
30. Lorenzi B, Mariani P, Reale A, Di Carlo A, Chen G, Narducci D. Practical development of efficient thermoelectric – photovoltaic hybrid systems based on wide-gap solar cells. *Appl Energy*. 2021;300:117343. doi:10.1016/j.apenergy.2021.117343
31. Ju X, Wang Z, Flamant G, Li P, Zhao W. Numerical analysis and optimization of a spectrum splitting concentration photovoltaic – thermoelectric hybrid system. *Sol Energy*. 2012;86:1941-1954. doi:10.1016/j.solener.2012.02.024
32. Lamba R, Manikandan S, Kaushik SC, Tyagi SK. Thermodynamic modelling and performance optimization of trapezoidal thermoelectric cooler using genetic algorithm. *Therm Sci Eng Prog*. 2018;6:236-250. doi:10.1016/j.tsep.2018.04.010
33. Lamba R, Kaushik SC. Thermodynamic analysis of thermoelectric generator including influence of Thomson effect and leg geometry configuration. *Energ Conver Manage*. 2017;144:388-398. doi:10.1016/j.enconman.2017.04.069
34. Yin E, Xuan Y. A novel optimal design method for concentration spectrum splitting photovoltaic–thermoelectric hybrid system. *Energy*. 2018;163:519-532. doi:10.1016/j.energy.2018.08.138
35. Bush KA, Palmstrom AF, Yu ZJ, et al. 23.6%-efficient monolithic perovskite/silicon tandem solar cells with improved stability. *Nat Energy*. 2017;2:1-7. doi:10.1038/nenergy.2017.9
36. Bjørk R, Nielsen KK. The performance of a combined solar photovoltaic (PV) and thermoelectric generator (TEG) system. *Sol Energy*. 2015;120:187-194. doi:10.1016/j.solener.2015.07.035
37. Najafi H, Woodbury K. Feasibility study of using thermoelectric cooling modules for active cooling of photovoltaic panels. Paper presented at: ASME 2012 International Mechanical Engineering Congress and Exposition; 2012:1-9.
38. Mahfoud A, Fathi M, Belghachi A, Djahli F. Numerical modeling of GaInP/GaAs monolithic tandem solar cells. *AIP Conf Proc*. 2016;1758:020014. doi:10.1063/1.4959390
39. Fernández EF, García-Loureiro AJ, Smestad GP. *Multijunction Concentrator Solar Cells: Analysis and Fundamentals*. Cham: Springer; 2015:9-37. doi:10.1007/978-3-319-15039-0_2
40. Meng F, Chen L, Sun F. Performance prediction and irreversibility analysis of a thermoelectric refrigerator with finned heat exchanger. *Acta Phys Pol*. 2011;120:397-406.

How to cite this article: Eke MN, Ibeagwu OI, Okoroigwe EC, Maduabuchi CC. Thermodynamic modeling of a spectrum split perovskite/silicon solar cell hybridized with thermoelectric devices. *Int J Energy Res*. 2022;1-16. doi:10.1002/er.8515